A Voltage Bias Effect on Catalytic Activity of Electrically Continuous Pt/TiO_2 Nanocomposites

Nathan J. Ray and Eduard G. Karpov*

Department of Civil and Materials Engineering, University of Illinois at Chicago, Chicago, Illinois, 60607, USA

KEYWORDS Mesoporous titania, controlled catalysis, plasma electrolytic oxidation, reaction current

Recently, efforts to optimize catalytic performance have included the utilization of catalytic nanoparticles with careful control over their shape and size, chemical composition, surface functionalization, and structural architecture. Here, we report direct measurements detailing the impact of applied external bias on the exothermic catalytic formation of water for a Pt/TiO_2 nanocomposite under exposure to gaseous oxyhydrogen environments. As external voltages of opposite polarity are applied to the system, the surface temperature kinetics, total pressure kinetics within the analytical chamber, and water turnover frequency transition in a reproducible manner between two well-defined states, resulting in (1) decreased catalytic activity, (2) decreased initial molecular adsorption onto the Pt catalyst, and (3) lower rates of water production under negative voltage. These findings pave the road toward the realization of a catalytic switch that can be activated by applying a voltage to Schottky barrier systems to enhance or mitigate catalytic surface reactions.

1. Introduction

Heterogeneous catalysis plays an instrumental role in everyday chemical processes, with applications too numerous to list. One emerging research interest that embraces the employment of a catalytic component is the field of catalytic nanodiodes. These nanocomposite devices have been shown adept at converting surface-released chemical energy supplied by reactions on the catalytic phase into chemical reaction-induced electrical signal.[1–8] One path toward optimization of these structures is tied to the optimization of the catalytic activity. To date, the need for catalytic activity optimization has been addressed primarily through the utilization of catalytic nanoparticles, with techniques such as control over shape and size[9–12], chemical composition[13], structural architecture[14], and surface functionalization[15,16] implemented to impact the rate of surface reactions. Advantageously, such morphological modifications have also been reported to enable selectivity during the catalytic reaction[9,11].

Application of an external voltage is an alternative method of catalysis control that has been investigated, with early results reported by Vayenas et al.[17] Oxide ions were supplied (removed) to the metal catalyst deposited on a ZrO_2(8 mol% Y_2O_3) substrate under applied positive (negative) voltage across the composite system. Additionally, Vayenas et al. demonstrated a similar effect existed within Na^+-conducting solid electrolytes such as β”-Al_2O_3. The impact of altering the concentration of oxide ions available at the metal catalyst surface led to an increase of the catalytic reaction rate up to 3×10^5 times higher than the rate of supply or removal of the oxide ions to the catalyst surface. They were able to illustrate that this effect depends on the controlled variation of the catalyst work function on polarization of the metal-substrate interface; moreover, the rate of the catalytic reaction displays an exponential dependence on the catalyst work function.

In a natural progression from oxide ions to electrons, Zhang et al. investigated the influence of variable electron density on the rates of redox reactions.[18,19] They utilized tin oxide nanowires in the configuration of a field-effect transistor; under this geometry, adsorption to or desorption from the nanowire by molecules significantly impacted the electron density of the SnO_2 nanowire along the reactive gas/nanowire interface under application of low gate voltages. The sensitivity of the catalytic activity of the nanowires to the electron density along the surface revealed the possibility of manipulation of the chemical reactivity and selectivity of catalytic reactions at the nanowire/reactive gas interface. This opened the door for prospective enhancement of catalytic reactions that involve charge transfer.

More recently, the adsorption of CO onto Pt/TiO_2 catalytic nanodiodes was investigated through the use of applied bias voltage studies. Taking advantage of the Pt/TiO_2 junction, Deshlahra et al. was able to control the electron transfer at the catalytic metal/semiconductor interface.[20] The applied voltage-induced electron transfer across the Schottky nanodiode was shown to directly impact the chemisorption of CO species in close proximity to the Pt/TiO_2 interface. This finding displays the potential for controlling surface chemical bonds by applying external voltages.

Here, we report on well-defined and reproducible switching behavior exhibited by $Pt/TiO_2/Ti$ nanocomposites as the exothermic catalytic reaction $H_2 + \frac{1}{2}O_2 \rightarrow H_2O$ occurs on the Pt phase. Under alternation between applied voltages of constant magnitude but opposite polarity across the Pt and Ti phases, an impact is observed in the surface temperature kinetics, total pressure kinetics within the analytical chamber, and water turnover frequency; all detected effects transition in a repeatable manner between two well-defined states. These two states will be shown to include different initial rates of molecular adsorption, different catalytic activities, and different rates of

water production. Moreover, surface temperature kinetics suggest the existence of two metrics that may be used to quantify the surface catalytic reaction during the exothermic reaction, namely the maximum surface temperature obtained, T_{max}, and the temperature time rate of change, $\dot{T}$.

2. Experimental Methods

TiO_2 films with a mesoporous morphology were grown on the parent metal titanium through a plasma electrolytic oxidation (PEO) process that has been reported elsewhere for these porous systems.[21–25] Research grade Ti metal with purity of 0.989 and dimensions of 36 × 12 × 0.5 mm^3 acted as the anode in an electrochemical cell, with a 153 × 26 × 6 mm^3 graphite cathode aligned parallel to the Ti, at a separation distance of 12 mm. Aqueous sulfuric acid (3M) was used as the electrolyte during galvanostatic oxidation of Ti with a current density of 93.2 $mA \cdot cm^{-2}$. This setup was placed into a 4.5 L water bath maintained at room temperature to function as a heat sink. After three minutes of the PEO process had elapsed, the applied voltage had increased to 95 V. At this point, the potential difference had surpassed the dielectric breakdown potential of the growing oxide film and consequently anodic spark discharge became visible along the TiO_2 surface. The resultant plasma reactions emanating from these discharges modify the TiO_2 morphology through their high localized temperature and pressure, producing self-assembled mesoporous morphology that is homogeneous on the macroscale. As the underlying Ti oxidation mechanism is the conversion of the substrate metal into its oxide by means of growth both inward and outward, there is a high degree of adhesion between the Ti substrate and the TiO_2 film. The voltage reached a stable value of 150 V after 15 min, approaching 155 V ± 2 V in the following 5 min. The oxidation procedure was aborted abruptly after 20 min, resulting in a primarily rutile phase mesoporous TiO_2 layer of thickness 10 – 11 μm.[21,24]

A metal-semiconductor heterojunction was then fabricated by deposition of 0.9995 purity Pt onto the free TiO_2 surface through a 34 × 10 mm^2 mask via wide-angle physical vapor deposition at a constant rate of 0.02 $nm \cdot s^{-1}$. This as-deposited Pt layer forms an electrically continuous nanogranular mesh-like structure, with the Pt growth monitored by an Inficon quartz microbalance throughout the deposition process. When the Pt film reached a thickness of 15 nm, the deposition was terminated by closing the source shutter.

SEM micrographs of the Pt/TiO_2 surfaces are shown in Figure 1. Panels (A) and (B) display the uncoated TiO_2 and Pt-coated TiO_2 nanocomposite, respectively, with Figure 1 (B) exhibiting the nanogranular topography the Pt film assumes. Figure 1 (C) reveals the macroscale homogeneity of the PEO-induced porosity; the regions of clearly identifiable different brightness levels correspond to the Pt-coated and uncoated regions of TiO_2. Comparison of (A) to (B), accompanied by closer inspection of (C), reveals that the surface morphology is not altered significantly during the Pt deposition process, confirming that the Pt layer thus forms a mesh-like topography. Nanogranular in structure, DC resistance measurements reveal in-plane electrical continuity across the Pt phase. SEM-grade silver paste was then used to fasten 0.25 mm diameter silver wires to the ends of the Pt mesh, resulting in 2.8 cm^2 of exposed Pt that served as the effective active area to support catalytic surface reactions.

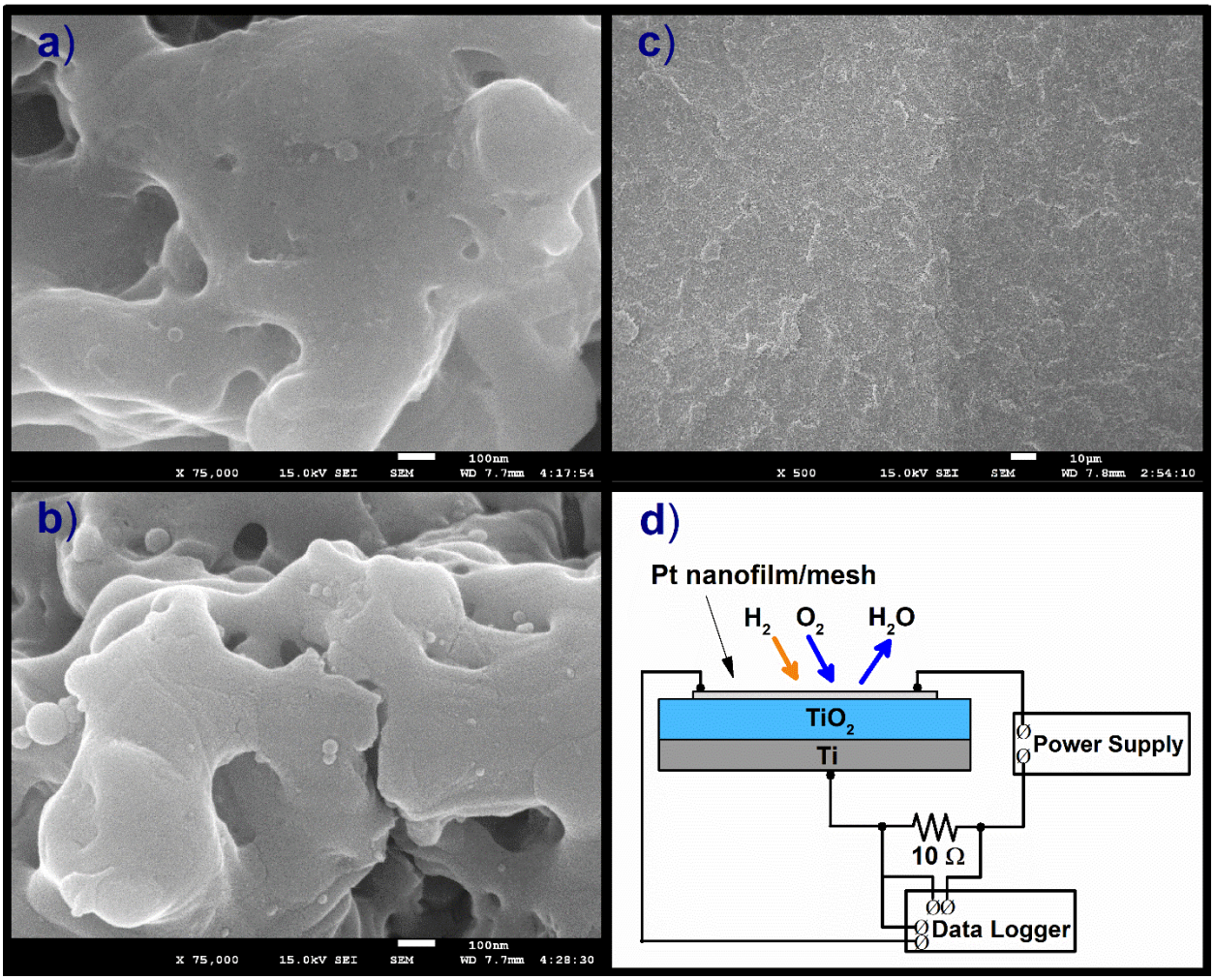

Figure 1. SEM images of Pt/TiO_2 nanocomposite. Panel (A) depicts TiO_2 prior to Pt deposition, while (B) reveals the nanogranular topography of the Pt deposition on TiO_2. Panel (C) presents the interface between Pt-coated and uncoated TiO_2, while (D) is a schematic for the experimental setup used.

A Pt resistive temperature detector (Omega F2020−100) was positioned onto the center of the Pt phase under the support of its connection wires only to avoid the use of adhesives that may introduce contaminants. Following the placement of the Pt temperature sensor, the fabricated samples were placed into a 4.5 L analytical vacuum chamber with residual gas pressure $< 10^{-6}$ Torr. The current-voltage characteristics for these structures have been reported under different gas environments previously and have been shown to exhibit *n*-type Schottky diode-like response under exposure to oxyhydrogen environments.[21] As the surface reaction

$H_2 + \frac{1}{2}O_2 \rightarrow H_2O$ occurs, a chemical electromotive force is induced in the device across the potential barrier at the Pt/TiO_2 interface. This chemically-induced emf drives current through an external circuit connected to the device, therein enabling electrical power generation. Even more remarkably, a secondary mechanism exists at the mesoporous metal/semiconductor interface that promotes *room-temperature* power generation long after the initial surface temperature increase due to the exothermic hydrogen oxidation has abated.

3. Results and Discussion

The present work explores the possibility of applying an external bias to the samples to either enhance or mitigate the surface reaction. A depiction of the sample geometry and the external circuit used during applied bias experiments is shown in Figure 1 (D). Analytical chamber pressure, sample surface temperature, and reaction-induced current kinetics are displayed in Figure 2 in the absence of an applied external voltage. As indicated in the inset, the reaction current was routed through a load resistance and the potential drop across that resistor was recorded, with the (+) V terminal on the electrically continuous Pt phase. All measurements were conducted in batch reactor mode, with gas admittance executed diffusively at a rate of 2−3 Torr·s^{-1}. At the time indicated by the first vertical dashed line in Figure 2, 160 Torr O_2 was added the analytical chamber. Following a waiting period of 1−2 min to allow for thermal equilibrium, 16 Torr H_2 was administered to the chamber; this is illustrated by the second vertical dashed line in Figure 2. At the onset of the catalytic reaction, immediately following the addition of hydrogen, the current displays a negative polarity as pre-adsorbed oxygen species are reduced. The current then decreases in magnitude and reverses polarity through the generation of thermionic emission as the surface temperature increases due to the exothermicity of the surface reaction. Ultimately, the current reduces in magnitude and reverses polarity yet again as the sample returns to room

temperature, remaining in a negative-polarity regime for the duration of the experiment and continuing to produce electrical power long after the sample surface returned to room temperature. The kinetics and mechanisms throughout this process have been carefully analyzed and reported by Karpov et al. previously.[21] Each measurement experiment, see Figure 2, was allowed to proceed about 30 min after the addition of H_2, after which the analytical chamber was evacuated.

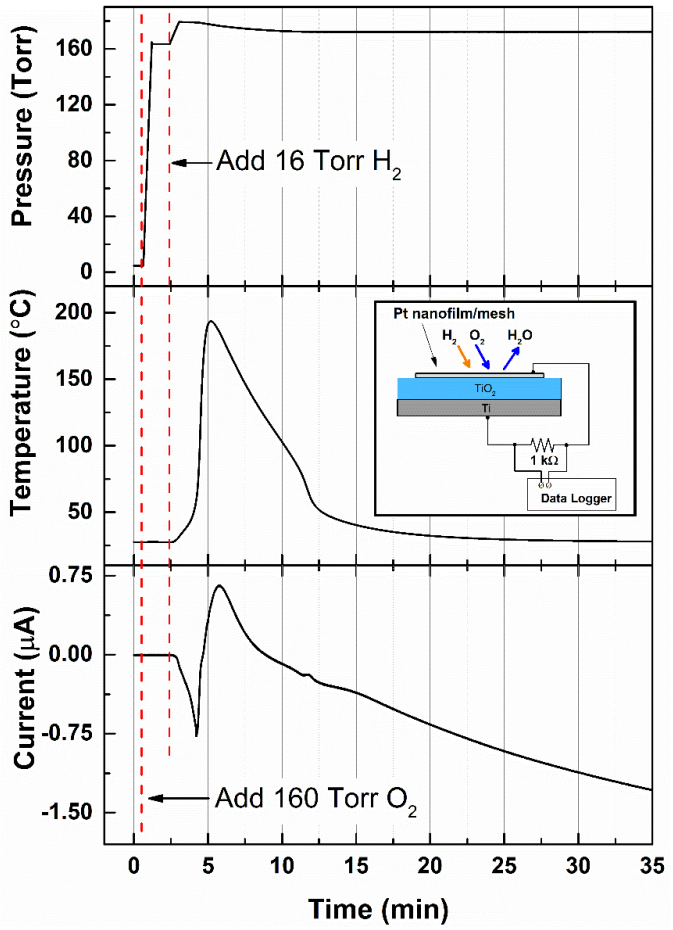

Figure 2. Pressure, temperature, and reaction current kinetics from $Pt/TiO_2/Ti$ system due to the addition of O_2 and H_2 to an analytical chamber initially held under vacuum; the vertical dashed lines indicate the addition of O_2 and H_2. The inset displays the external circuit used to record the reaction current, with the (+) V terminal on the Pt phase.

For the findings reported here, a slightly modified setup was implemented, see Figure 1 (D). A high precision power supply was introduced to the system; under this new configuration the current through the sample, surface temperature, total pressure within the analytical chamber, and partial pressures of sampled volumes of the gas mixture were recorded simultaneously. The applied voltage and current compliance settings were maintained such that the electrical power contributed to the sample never exceeded 100 mW; in this regard the heating due to power dissipation can be assumed negligible relative to the exothermic chemical reaction. The temperature kinetics for a Pt/TiO_2 system under cyclic exposures to the described oxyhydrogen environment of 160 Torr O_2 and 16 Torr H_2 are given in Figure 3. Constant voltages of magnitude 2.4 V were applied to the Pt phase according to the experimental setup shown in Figure 1 (D), with polarity indicated in the plot legend. In the time between experimental trials, labeled Exp. #1, Exp. #2, etc. in the legend and conducted in chronological order, the chamber was pumped out to obtain the initial vacuum state; additionally, the sample surface temperature was ensured to be at room temperature prior to the initiation of all experiments, as seen in the inset of Figure 3. The procedure of adding O_2 and H_2 remains unchanged from the data depicted in Figure 2, with the x-axis time-shifted such that time t = 0 min corresponds to the addition of hydrogen to the analytical chamber. The pressure of hydrogen added and rate of hydrogen addition were maintained constant across all six experiments, resulting in the addition of 16.12 ± 0.02 Torr H_2 at a rate of 23.56 ± 0.19 Torr·min^{-1}; these values correspond to relative standard errors of 0.14% and 0.81% for volume of H_2 added and the rate at which it was added, respectively.

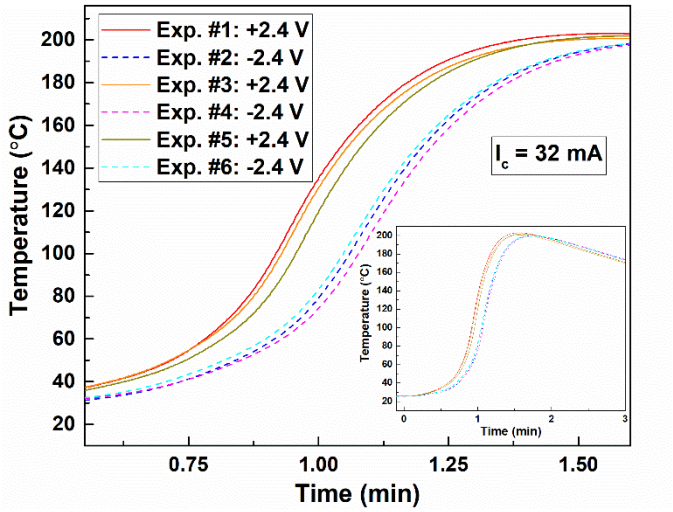

Figure 3. Surface temperature kinetics of Pt phase during catalytic surface reaction. The listed voltages were applied to the Pt phase, with the experiments occuring in chronological order as indicated in the legend. Inset displays the same data on larger time scale.

Analysis of the temperature kinetics reveals a clear switching behavior as the experiments are repeated, alternating between ±2.4 V with progressing experiments. Upon comparison of the positive and negative bias experiments depicted in Figure 3, it is seen that the apparent catalytic activity of the Pt phase changes with applied bias. Negatively-biased voltage to Pt modifies the catalytic performance such that it takes longer for the temperature to increase, indicative of a slower rate of water formation.

Examination of the rate of change of the temperature, $\dot{T}$, at the inflection point of the temperature curves in Figure 3 is displayed in Figure 4. This analysis shows that in the case of the negative bias, $\dot{T}$ was statistically significantly lower than that produced during the application of positively biased voltage. The error bars in Figure 4 were calculated as the standard error of $\frac{dT}{dt}$ obtained during positive and negative bias experiments. Upon further investigation it was seen that the maximum Pt temperatures obtained, see inset in Figure 3 for raw data, were in the range of

201.76 ℃ ± 0.6 ℃ for the +2.4 V experiments and 199.8 ℃ ± 0.02 ℃ for the -2.4 V experiments. As was the case with $\dot{T}$, the maximum temperature, T_{max} can also be explained by a decrease in water production induced by the applied negative bias. The findings from Figure 3 and Figure 4 suggest that there are two metrics obtained from surface temperature measurement data that may be used to quantify the catalytic reaction, i.e. T_{max} and $\dot{T}$.

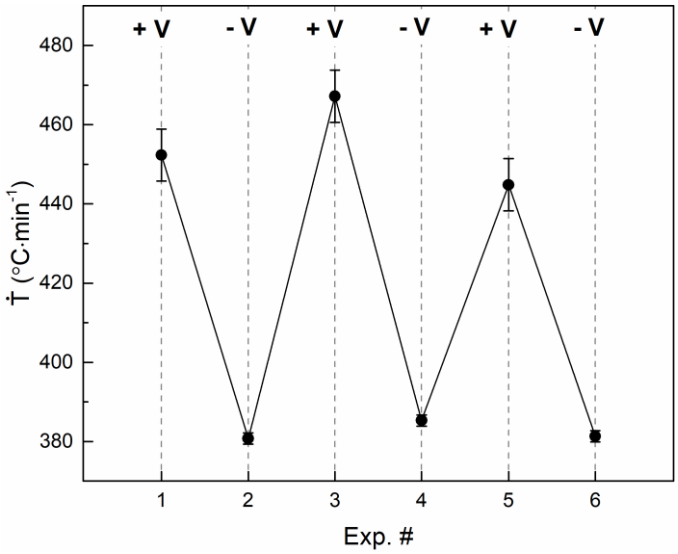

Figure 4. Temperature rates of change evaluated at the inflection point of the temperature curves shown in Figure 3 during application of ±2.4 V, with the bias applied during each experiment indicated above the dashed line.

The total pressure kinetics immediately following the addition of H_2 to the analysis chamber offer further insight into the mechanics at play, see Figure 5. As seen in panel (A), time t = 0 min corresponds to the addition of 16 Torr H_2; prior to this point the sample was in a pure oxygen environment. Total pressure is indicated by the red plot, while current through the sample is given in the blue plot; the data acquisition device (+) V terminal is on the Pt. In the case of

panel (A), at the onset of H_2 addition there is a nonzero – albeit small – current under positive voltage to the Pt phase for this *n*-type Schottky diode. As more hydrogen is administered to the chamber, current through the sample begins to increase; the direction of flow is from the Ti substrate through the external circuit to the Pt phase, see the inset in Figure 5 (A). The power supply quickly switches to current compliance mode, remaining in this mode from $t = 0.5$ min – 0.8 min. At about $t = 0.65$ min the hydrogen addition has been completed, after which the pressure profile decays quasi-exponentially as H_2 adsorbs on the surface and initiates water formation, see Figure 2 for the full-length pressure kinetics. On the time scale depicted in Figure 5, however, this can be viewed as a linear process and the linear best fit is given as the dashed line. After 0.8 min, enough adsorbate species occupy the Pt surface to activate voltage compliance mode in the power supply, corresponding to the current decrease.

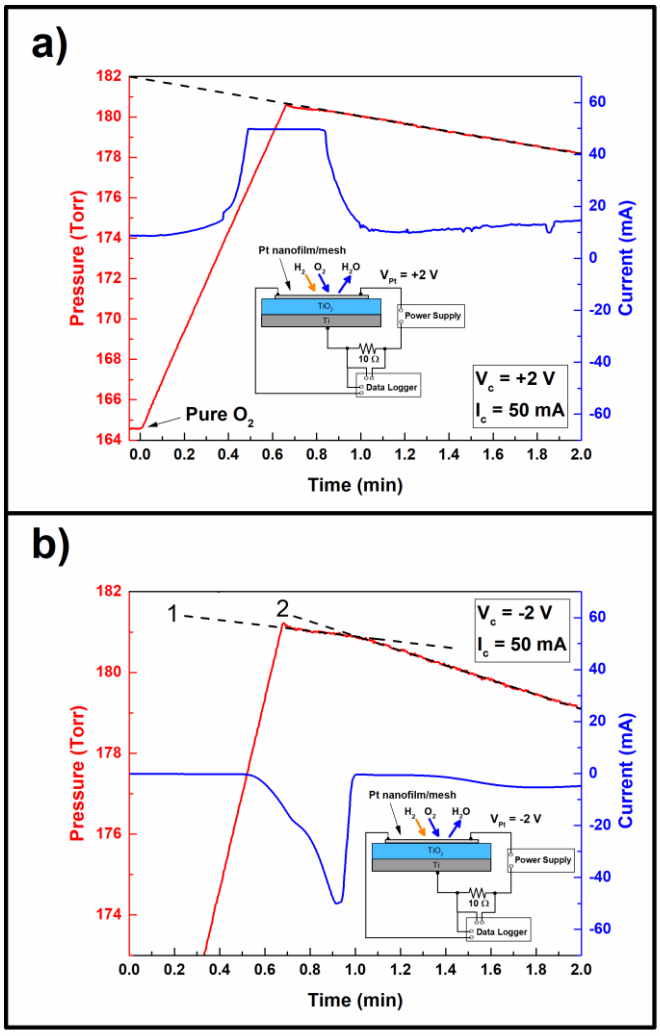

Figure 5. Total pressure kinetics within the analytical chamber and current kinetics through the sample under oppositely applied bias. The insets in each panel depicts the experimental setup, with current and voltage compliances indicated. The data acquisition device (+) V terminal is on the Pt phase.

Panel (B) in Figure 5, however, tells a different story. When applying a negative bias, the power supply does not enter into current compliance mode until 0.9 min, 0.2 min after the influx of hydrogen was terminated. The pressure data, meanwhile, makes a clear transition from one linear regime, referred to hereafter as the *shallow regime*, existing in the range 0.7 min – 1.0 min to that of another with a steeper (more negative) slope after t = 1.0 min; see the dashed lines for

the linear best fits of these regimes labeled as 1 and 2, respectively. Comparison of the best fit line from Figure 5 (A) to linear fit 2 in Figure 5 (B) revealed that the two cases ultimately converged to the same rate of change, with Ṗ differing by only 1.4% between the two cases.

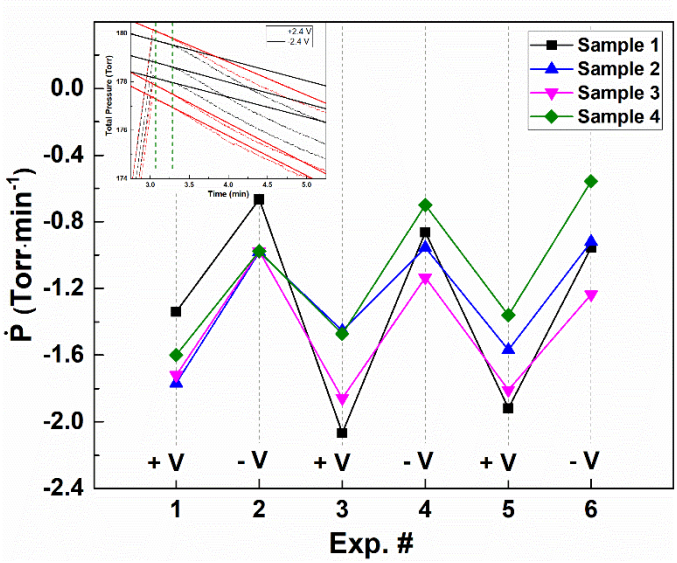

Figure 6. Pressure rate of change for ±V cyclic loading for four different samples. The inset depicts the best fit lines and gives a visual representation of the time window over which all slope values were calculated for a given experiment with 6 trials.

The different rates of change found in Figure 5 (B) prompted further investigation – analysis of the total pressure in the analytical chamber was conducted for four different samples, as represented in Figure 6. Investigation into each sample consisted of a total of six experiments − three trials with a positive voltage to the Pt phase, and three with negative bias to Pt. The data points were systematically generated in the following way: the data for the three negative bias trials were analyzed, and the run with the shortest shallow regime time was selected. This length of time was the parameter that was used to compute the linear best fittings for all six trials from which the slopes were obtained, see the inset in Figure 6 for a visual representation of

the this time window selection. The resultant plot in Figure 6 exhibits a clear and decisive zig-zag pattern as the applied voltage polarity is switched. This zig-zag pattern is indicative of complex surface mechanisms which limit adsorption from the gas phase for an initial period of 25 – 30 s, after which competing mechanisms dominate and adsorption proceeds uninterrupted. At present, the mechanism leading to the decreased adsorption of H_2 onto the Pt phase during the shallow regime under negative applied bias is not well understood. In the case of aqueous electrolytes interacting with Pt electrodes, obviously a more negative potential corresponds to an increase in H^+ adsorption as reported by Rodriguez et al.[26] Likewise, simulations conducted by Simonyan et al. produced a similar finding in the case of hydrogen adsorption onto carbon nanotube walls, i.e. negatively charged nanotubes induced more adsorption due to the positive quadrupole moment of hydrogen.[27] These results, however, conflict with our findings and a more detailed investigation is necessary to explain the dominant mechanism during the shallow regime.

To gauge whether the catalytic reaction is being effected, the rate of water production was examined. Water pressure was recorded in two different ways and is shown in Figure 7. The water pressure at a discrete time t = 20 min after the addition of hydrogen was calculated from the total pressure drop during that 20 min interval for each trial. For the reaction $\mathrm{H_2} + \frac{1}{2}\mathrm{O_2} \rightarrow \mathrm{H_2O}$, the water pressure produced can be derived from the total pressure data according to

$$\Delta P = \Delta P_{H_2} + \Delta P_{O_2} + \Delta P_{H_2O} \quad (1)$$

by relating the pressure decreases as H_2 and O_2 are consumed to the pressure increase during H_2O production and implementing the known boundary conditions $\mathrm{P_{H_2O}} = 0$ Torr, $\mathrm{P_{H_2}} = 16$ Torr, and $\mathrm{P_{O_2}} = 160$ Torr. As a second method of verification, the inset in Figure 7 displays partial pressure data obtained via mass spectrometry measurements of sampled gas volumes that have been averaged across the three positive voltage trials and the three negative voltage trials.

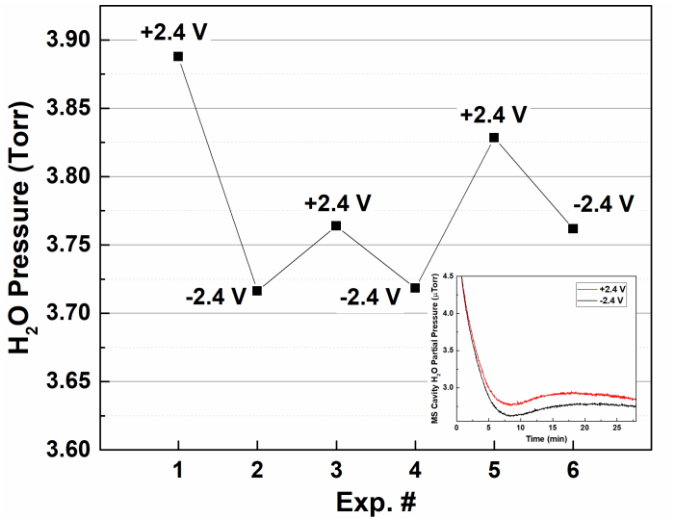

Figure 7. Water pressure produced under oppositely applied bias. Inset gives partial pressures recorded by mass spectrometry averaged across the three +2.4 V trials and the three -2.4 V trials.

As is evident by both sets of data found in Figure 7, the quantity of water produced is directly influenced by the external bias applied. This serves to verify that the applied bias, observed to impact both the temperature kinetics and the total pressure kinetics, does have bearing on the rate of water production. The water turnover frequency, observed to be lower for negative voltage applied to Pt when compared to the preceding or following experiment with positive voltage, may be explained on the basis of elementary adsorbate species interactions. The adsorption of hydrogen on a platinum surface is widely accepted to follow the Tafel-Volmer mechanism for hydrogen oxidation on Pt electrodes[28],

$$H_2^{gas} + 2Pt \leftrightarrow 2H^{ads} \quad (2)$$

$$H^{ads} \leftrightarrow H^+ + Pt + e^- \quad (3)$$

The adsorbed hydrogen ions are then free to participate in the standard cathodic fuel cell reaction[29],

$$O_2 + 4H^+ + 4e^- \rightarrow 2H_2O \quad (4)$$

But the Pt/TiO_2 interface includes a Schottky barrier with depletion layer width that can be given, in the case of an ideal planar junction under the depletion approximation, by[20]

$$x_d = \sqrt{\frac{2\,\varepsilon_s\,(\phi_i - V_a)}{q\,N_d}}, \tag{5}$$

where ε_s is the permittivity of TiO_2, q is the charge of an electron, ϕ_i is the built-in potential across Pt/TiO_2 interface (positive for *n*-type TiO_2), V_a is the applied external voltage, and N_d is the carrier density of the TiO_2. From this expression, it is obvious that the depletion region thickness will decrease with a positive bias, and increase when a negative bias is applied to the Pt phase. The electric field corresponding to this charge depletion layer will experience its maximum along the Pt/TiO_2 junction, and can be expressed as

$$\mathcal{E}_{max} = \frac{q\,N_d\,x_d}{\varepsilon_s} \tag{6}$$

It follows that, for larger charge carrier depletion layers, there is a greater electric field that is generated along the Pt/TiO_2 interface. For the production of water given by Equation (4), the electric field represented by Equation (6) will serve drive H^+ away from the interface, therein inhibiting the rate of water production in a volume within close spatial proximity to the interface. This is manifested both through the temperature kinetics depicted in Figure 3, as well as the water turnover frequency in Figure 7. This results emphasizes the importance of the mesoporous morphology of the Pt/TiO_2 system investigated – with such a highly porous substrate, the triple phase Pt/TiO_2/reactive gas interfacial length is significantly longer than would be the case for Pt deposition onto a planar substrate. The effect is short-lived, apparently ended by the population of the surface with a surplus of adsorbate species. At the conclusion of the shallow regime, the Pt/reactive gas interface is inhabited with enough adsorbed hydrogen species to negate the impact

the negative bias has on water production. Surface characterization techniques are needed to confirm this mechanism as the mitigating factor for water production.

4. Conclusions

We conclude that Pt/TiO_2/Ti nanocomposite heterojunctions, which have been demonstrated adept at conversion of surface-released chemical energy into stationary room-temperature power generation under oxyhydrogen exposure, can also be harnessed to impact the rate of water production during this catalytic reaction through simple application of a potential difference across the Pt and Ti phases. This remarkable finding represents the realization of a *catalytic switch* that can be activated by applying a voltage to the system to either enhance or mitigate the surface reaction. In the cases of applying constant voltage, equal in magnitude but opposite in polarity, across the Schottky barrier, the surface temperature kinetics, total pressure kinetics, and water turnover frequency have all been shown to transition in a reproducible manner between two well-defined states. Relative to positive bias, negative bias to the Pt phase induces: 1) decreased catalytic activity as observed in the surface temperature profile, 2) a period of time during which molecular adsorption of hydrogen onto the Pt catalyst is reduced, and 3) lower rates of water production. From surface temperature measurements, both T_{max} and $\dot{T}$ can be used to quantify the catalytic surface reaction. The mechanism responsible for this interchanging behavior due to oppositely applied biases needs to be thoroughly investigated so that this controlled catalysis mechanism can be implemented, significantly impacting the dynamics within the field of catalysis.

AUTHOR INFORMATION

Corresponding Author

*E-mail: nray7@uic.edu

ACKNOWLEDGMENT

This research was supported by the Center for Nanoscale Materials at Argonne National Laboratory. Use of the Center for Nanoscale Materials, an Office of Science user facility, was supported by the U.S. Department of Energy, Office of Science, Office of Basic Energy Sciences, under Contract No. DE-AC02-06CH11357.

REFERENCES

[1] U. Hagemann, M. Timmer, D. Krix, P. Kratzer, H. Nienhaus, *Phys. Rev. B* **2010**, *82*, 155420.

[2] U. Hagemann, Hermann Nienhaus, *New J. Phys.* **2014**, *16*, 113035.

[3] J. Y. Park, S. M. Kim, H. Lee, I. I. Nedrygailov, *Acc. Chem. Res.* **2015**, *48*, 2475.

[4] I. I. Nedrygailov, E. G. Karpov, *Sensors Actuators, B Chem.* **2010**, *148*, 388.

[5] H. Lee, I. I. Nedrygailov, C. Lee, G. A. Somorjai, J. Y. Park, *Angew. Chemie Int. Ed.* **2015**, *54*, 2340.

[6] H. Lee, I. I. Nedrygailov, Y. K. Lee, C. Lee, H. Choi, J. S. Choi, C.-G. G. Choi, J. Y. Park, *Nano Lett.* **2016**, *16*, 1650.

[7] J. Y. Park, G. A. Somorjai, *ChemPhysChem* **2006**, *7*, 1409.

[8] J. Y. Park, J. R. Renzas, A. M. Contreras, G. A. Somorjai, *Top. Catal.* **2007**, *46*, 217.

[9] C. Tsung, J. N. Kuhn, W. Huang, C. Aliaga, L.-I. Hung, G. A. Somorjai, P. Yang, *J. Am. Chem. Soc.* **2009**, *131*, 5816.

[10] S. H. Joo, J. Y. Park, J. R. Renzas, D. R. Butcher, W. Huang, G. A. Somorjai, *Nano Lett.* **2010**, *10*, 2709.

[11] S. Kundu, S. Lau, H. Liang, *J. Phys. Chem. C* **2009**, *113*, 5150.

[12] J.-Y. Park, Y.-J. Lee, P. K. Khanna, K.-W. Jun, J. W. Bae, Y. H. Kim, *J. Mol. Catal. A Chem.* **2010**, *323*, 84.

[13] Ö. Metin, X. Sun, S. Sun, *Nanoscale* **2013**, *5*, 910.

[14] B. Rungtaweevoranit, J. Baek, J. R. Araujo, B. S. Archanjo, K. M. Choi, O. M. Yaghi, G. A. Somorjai, *Nano Lett.* **2016**, *16*, 7645.

[15] J. Huang, L. Zhang, B. Chen, N. Ji, F. Chen, Y. Zhang, Z. Zhang, *Nanoscale* **2010**, *2*, 2733.

[16] J. Y. Park, C. Aliaga, J. R. Renzas, H. Lee, G. A. Somorjai, *Catal. Letters* **2009**, *129*, 1.

[17] C. G. Vayenas, S. Bebelis, S. Ladas, *Nature* **1990**, *343*, 625.

[18] Y. Zhang, A. Kolmakov, S. Chretien, H. Metiu, M. Moskovits, *Nano Lett.* **2004**, *4*, 403.

[19] Y. Zhang, A. Kolmakov, Y. Lilach, M. Moskovits, *J. Phys. Chem. B* **2005**, *109*, 1923.

[20] P. Deshlahra, W. F. Schneider, G. H. Bernstein, E. E. Wolf, *J. Am. Chem. Soc.* **2011**, *133*, 16459.

[21] E. G. Karpov, M. A. Hashemian, S. K. Dasari, *J. Phys. Chem. C* **2013**, *117*, 15632.

[22] S. Fullam, N. J. Ray, E. G. Karpov, *Superlattices Microstruct.* **2015**, *82*, 378.

[23] N. J. Ray, M. A. Hashemian, E. G. Karpov, *ACS Appl. Mater. Interfaces* **2015**, *7*, 27749.

[24] N. J. Ray, E. G. Karpov, *ACS Appl. Mater. Interfaces* **2016**, *8*, 32077.

[25] N. J. Ray, V. V. Styrov, E. G. Karpov, *Chem. Phys. Lett.* **2017**, *689*, 111.

[26] J. M. Doña Rodríguez, J. A. Herrera Melián, J. Pérez Peña, *J. Chem. Educ.* **2000**, *77*, 1195.

[27] V. V. Simonyan, P. Diep, J. K. Johnson, *J. Chem. Phys.* **1999**, *111*, 9778.

[28] X. Jiao, C. Lin, N. P. Young, C. Batchelor-McAuley, R. G. Compton, *J. Phys. Chem. C*

2016, *120*, 13148.

[29] T. Jacob, W. A. Goddard, *ChemPhysChem* **2006**, *7*, 992.